Ions transmitted through an anodic nanocapillary array

H. F. Krause, C. R. Vane, and F. W. Meyer
Physics Division, Oak Ridge National Laboratory, P.O. Box 2008, Oak Ridge, Tennessee 37831-6372, USA
(Received 18 July 2006; revised manuscript received 9 January 2007; published 17 April 2007)

The transmission of incident 10–20 keV/q Ar^{+}, Ar^{3+}, Ne^{3+}, and Ne^{7+} ions in an Al_2O_3 nanocapillary array was studied. The array consists of a dense distribution of pores typically 100 nm in diameter and 60 μm in length. Emergent charge-state-selected angular distributions were studied at low energy using a two-dimensional (2D) position sensitive detector. The principal transmitted q state is the incident q state in all cases. The transmitted fraction of incident beam, $\approx 2\times 10^{-8}$, is many orders of magnitude smaller than the array's surface porosity ($\approx$40%). No evidence of significant energy loss is observed for the transmitted ions. Yields in lower q states and neutrals formed by electron capture are typically below 3% of the entrance q-state yield. Observed angular distributions consist of well resolved, 2D structures sitting on a continuum distribution. The angular distribution and sharp angular structures can be steered in the direction of the pores within about ±0.5° without a significant loss of transmitted intensity by rotating the sample with respect to the incident beam. All data suggest that the structure in the scattered ion angular distributions arises when ions bounce at ultralow grazing angles in very large impact parameter Coulomb collisions with electrically charged nanopore walls. Analysis of the observed structure has allowed the identification of single, double, and triple collisions inside the nanopores.

DOI: 10.1103/PhysRevA.75.042901 PACS number(s): 61.85.+p, 32.80.Fb, 34.50.Fa, 79.20.Rf

I. INTRODUCTION

For more than 15 years, considerable effort has been directed toward producing and studying the properties of very small pores or capillaries in thin self-supporting insulator membranes [1]. Increased interest in nanotechnology, and the desire to probe the physical and chemical properties of these porous arrays motivated the application of a wide variety of analytic techniques [1,2]. An increasing amount of information about the characteristics of nanoporous targets resulting from different production techniques is now becoming available.

The transmission of slow, highly charged ions (HCIs) through nanocapillary targets is the most recent tool employed to probe the interior of nanopores [3–9]. Short capillaries (1–10 μm) in a Al_2O_3 substrate were investigated by Yamazaki *et al.* [3] using 2–4 keV/u HCI beams. This work was directed toward the study of electron capture and ionization processes, and the formation of highly excited "hollow atoms," using the subsequent x-ray emission that occurs when HCIs undergo ultragrazing collisions with nanopore walls. Capillaries having a diameter and length of 250 nm and 1.5 μm, respectively, in a Ni foil and also in an Al foil were studied later [4,5]. Theoretical studies concerning the transmission of HCIs in short metallic pores quickly followed [6].

Studies of ion transmission through low porosity (1–10 %) insulating carbonaceous capillary targets were initiated most recently using slow incident HCIs [7–9]. The nanopores used in these studies were produced by etching ion tracks formed after energetic xenon HCIs (several hundred MeV) strike thin polyethylene terephthalate (PET) or mylar films. The experiments studied the transmission of incident 3 keV Ne^{7+} ions (0.35 keV/u) in 100-nm-diam capillaries having a length of 10 μm, which cover about 4% of the target surface area. Stolterfoht *et al.* [7,8] observed a surprisingly large fraction of the incident charge state ($\approx$50%) for ions transmitted when the axis of the pores was aligned close to the beam direction. The insulator films typically had a 30 nm Ag or Au film deposited on the entrance and exit surfaces but uncoated samples were also investigated. The measured angular distribution was found to be smooth and broad (4–6° FWHM) and centered on the axis of the nanopore direction. The transmitted ion fraction in lower exit charge states (resulting from electron capture in pores) was found to be small ($\approx$1%). The slow HCIs appeared to be "guided" through the pores without touching the internal walls by electrical charges deposited on the nanopore walls. Other aspects of the "guided ion" phenomena in these thin carbonaceous films were also studied [9–13] and these films continue to be the subject of experimental and theoretical investigation for low-energy ions by several groups (Yamazaki *et al.* [10], Aumayr *et al.* [11], and Burgdörfer *et al.* [12]). Investigations of slow ion transmission through low porosity, regularly spaced short pores in a SiO_2 substrate by Schuch *et al.* are also in progress [13].

Our interest in probing nanocapillary targets using HCIs at substantially higher impact energies (i.e., 20 keV/q and initially at 200 MeV) arose from our background in ion channeling where swift ions travel in solids between rows and sheets of target atoms in crystals via distant repulsive electromagnetic interactions [14]. Recent theoretical calculations predicting the scattering of ions in ordered nanotube targets intensified that interest [15]. We selected a high porosity ($\approx$40%) and relatively thick aluminum oxide array because this type had not been studied using ion scattering techniques, and because a large amount of information gathered using other diagnostic techniques is available [1,2]. These commercial membranes, which have a reproducible pore structure and a narrow pore size distribution ordered in a hexagonal pattern, are produced by the anodic oxidation of aluminum. Samples having long-range ordering have also

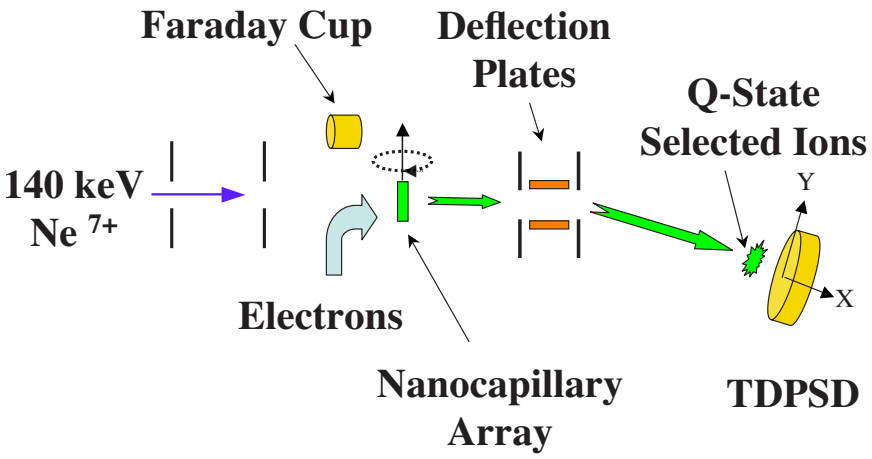

FIG. 1. (Color online) Schematic diagram of the low-energy experimental apparatus (not drawn to scale). When the nanocapillary target is rotated clockwise from above about an axis in the vertical direction then the transmitted ions move along the $+X$ direction fixed in the detector coordinate system shown. Important apparatus dimensions are given in Sec. II B.

been produced [16]. Interest in these membranes has already resulted in applications in a wide range of gas and liquid biofiltration and separation, including microfluidics. Because of ongoing research, new devices using alumina substrates are now envisioned, such as memory storage devices [16], microwave guides [17], and electromagnetic gratings. Use of porous arrays as a base template for producing freestanding aligned nanotubes has been discussed as well [18,19].

Unlike previous work, our studies focus on the transmitted charge-state-selected angular distributions at high angular resolution using 10–20 keV/q projectile ion beams of Ar^{+}, Ar^{3+}, Ne^{1+}, Ne^{3+}, and Ne^{7+}. This is also the first set of nanopore target studies where the incident beam is essentially parallel ($<0.02°$ FWHM). To our surprise, the thick alumina targets studied exhibit a very complicated but understandable angular distribution for transmitted ions. Our work also demonstrates that these arrays can be used as beam attenuators for HCI beams in the low-intermediate energy regime (i.e., ions in the few keV to 500 keV energy regime) because most of the transmitted ions do not undergo significant energy loss or a change in charge state. This work is part of the larger beam-surface effort at the ORNL Multicharged Ion Research Facility (MIRF) that seeks to develop a fundamental understanding of neutralization, energy dissipation, and sputtering processes occurring when slow or intermediate energy HCIs interact with metal, semiconductor, and insulator surfaces.

II. EXPERIMENTAL APPROACHES

A. Nanopore target

The Al_2O_3 capillary array (Whatman, Inc., Anodisc 13), which is rigid and self-supporting, consists of a dense distribution of nanopores with a precise honeycomb structure. The pore diameter D and average length L are specified by the manufacturer to be 100 nm and 60 μm, respectively (aspect ratio, $D/L=1/600$), distributed over a disk diameter of 13 mm [20]. The array has a fractional open area of about 40%, corresponding to a pore density of about $3\times10^{9}/\mathrm{cm}^{2}$, which is about 10–20 times higher density than that of polycarbonate targets studied by Stolterfoht *et al.* and others [3–13].

Alumina arrays, sometimes called "Anopore" membranes in the literature, are produced by anodic oxidation of an aluminum film. Because the process is electrochemical, formation conditions can be precisely controlled and a reproducible pore structure with a narrow pore size distribution is obtained. These targets have been extensively studied in separate investigations using scanning electron microscopy (SEM), gas absorption techniques, deuterium magnetic resonance (NMR), and small-angle neutron scattering, and the results show that the uniform size pores are smooth, straight, and arranged in a pseudohexagonal pattern [1,2]. More information about anodic processing, the array characteristics, and characteristics of the nanopores is available [1,2,16,19]. Comparative results using the same diagnostics on polycarbonate nanotargets, similar to those used by Stolterfoht *et al.*, are also discussed [1].

B. Low-energy studies

Initial investigations of ion transmission and energy loss through the porous Al_2O_3 target were performed using a 200 MeV Ti^{+12} ion beam to determine the alignment direction and assess whether the nanopores are sufficiently coaligned to justify further investigations [21]. We chose to measure projectile energy loss at high velocity because no insulator target can become sufficiently charged electrically to prevent passage of such energetic ions. By measuring the transmitted intensity of ions having relatively low-energy loss vs beam-target alignment in goniometer tilting experiments, we found that an upper limit to the 2D dispersion of nanopore longitudinal directions is less than 1.6° full width at half maximum (FWHM) in a direction perpendicular to the surface of the nanopore array. This degree of nanopore misalignment was considered sufficiently low to warrant meaningful studies at much lower ion energy.

Low-energy studies were performed at the ORNL MIRF using a setup shown schematically in Fig. 1. Incident 10–20 keV/q Ar^{+}, Ar^{3+}, Ne^{3+}, and Ne^{7+} ions were produced by the CAPRICE electron cyclotron resonance (ECR) ion source. The HCI beam, selected by magnetic analysis and small collimating slits, was highly collimated and tuned to be essentially parallel ($\approx0.02°$ measured beam divergence) before it impinged on the capillary array mounted in the goniometer. The two beam defining apertures sketched in Fig. 1, typically having a diameter of 0.5 mm, were separated by

3.40 m to achieve this low beam divergence. Ions emerging from the array were deflected vertically using electrostatic analysis so that final q state selected angular distributions could be fully separated and also distinguished from any in-line neutrals. The electrostatic plates (7.6 cm length separated by 2.5 cm) did not limit the range of angular distribution measurements in the vertical direction for any projectile beam studied. The electric field lines from the plates, which were oppositely and symmetrically biased with respect to ground, terminated on vertical grounded plates as shown in Fig. 1; this minimized stray longitudinal electric fields in the target or the detector directions. Resultant two-dimensional (2D) angular distributions were measured using a 2.5-cm-diam high-resolution TDPSD located 78 cm from the target. The multichannel plate detector outfitted with a resistive anode had a total angular acceptance of $\approx \pm 0.9°$ and an angular resolution $\Delta\vartheta \approx 8 \times 10^{-3}$ degrees in the X or Y directions. The detector, rotated about 9.5° below the beam line in a vertical plane for charge state separation, could also be rotated in the horizontal plane to measure ions scattered beyond the detector's angular acceptance in the horizontal direction. Vacuum throughout the experimental apparatus was typically 5×10^{-8} Torr during the experiments.

To partially control electrical charging of the target (insulator) during projectile ion impact for low-energy beams, a high-transmission ($\approx 90\%$) grounded electroformed grid (100 lines/cm Mo) was mounted on the entrance side of the array. The capillary array and mesh were mounted in a precision goniometer so that transmitted ion intensity vs sample orientation could be studied easily even in high-energy projectile impact experiments. During experiments, the target entrance grid was used to monitor the relative variations in the incident HCI beam current. The wire mesh was also used to measure the current of low-energy electrons (<4 eV), flooding the target when they were used to neutralize charge buildup on the front side of the array. The Faraday cup shown in Fig. 1 (outfitted with a biased suppressor grid) was used to measure incident beam currents accurately.

III. RESULTS: 140 keV Ne^{7+}

A. Procedure

Although we have also studied the interesting characteristics of nanopore samples having Au film cladding [22], all results discussed in this paper were obtained without any metallic films deposited on the entrance and exit surfaces. Initially, a low-intensity incident beam ($<10^{-14}A$) was observed on the in-line TDPSD with the target array removed to locate the beam direction and measure its angular width. With the array inserted (a virgin target sample), the beam intensity was gradually increased to observe transmitted ions on the TDPSD. An incident beam current below 10 nA was used in most experiments for a beam of 1- or 1/2-mm-diam so the incident beam sampled about 8×10^6 and 2×10^6 pores, respectively. At this low incident beam current, less than one ion is inside a pore at any time (i.e., about $0.3/q$ ions/μs/pore, where q denotes the incident charge state). To align the pores of the anodic array with the beam, two orthogonal rotational motions of the goniometer were then adjusted so that the centroid of the transmitted angular distribution matched the incident beam direction. After some experience, we learned that this alignment procedure maximized the number of transmitted ions per particle nA of incident beam (i.e., the number of pores oriented in the incident beam direction). Once alignment was achieved, the electrostatic analyzing field was established and the TDPSD was rotated vertically downward to select an exit q state of interest that had been deflected by the electrostatic plates after the target (see Fig. 1).

B. Transmitted Charge States and Yields

In general, transmitted angular distributions for each projectile species, charge state, and beam energy studied are found to be remarkably similar. Like findings reported on much thinner PET film targets at very low incident energy by Stolterfoht *et al.* [7–9] and other groups [10–13], the predominant charge state transmitted in our target is always the incident charge state species. The ion yield in lower charge states, which can only occur if the projectile captures one or more electrons from the target array, is always found to be below a few percent of transmitted intensity of the incident q state for each beam energy or target alignment used. Unlike lower-energy results obtained using 10-μm-thick PET films [3–11], the transmitted ion signal is typically about 2×10^{-8} of the measured particle nA beam current incident on the array. This yield corresponds to a transmitted fraction of $\approx 6 \times 10^{-7}$, assuming that the fractional transmission of the metallic grid and the target porosity are 90% and 40%, respectively. The transmitted fraction is found to be essentially independent of the incident beam energy, charge state, projectile species, and less well collimated incident beams in the aligned condition. However, the fraction decreases substantially when the target is rotated by several degrees in either direction from the "best alignment" position. The measured yield is also independent of small voltages (±25 V) applied to the mesh mounted on the front of the alumina capillary array and there is no evidence that transmitted ions experience significant energy loss in the percent range. The measurement of high-resolution energy loss ($R > 10^3$) is not possible in the present experimental configuration.

C. Angular distributions

Figure 2 shows a $2° \times 2°$ isometric view of the angular distribution for 140 keV Ne^{7+} ions incident on and emerging from the capillary target best aligned to the incident beam direction. Surprisingly, the 2D angular distribution consists of many narrow peaks sitting on a continuum when viewed at our high angular resolution. This is a steady-state distribution acquired after the incident beam irradiated the target for at least ten minutes, following an observed transient buildup of the transmitted intensity (later discussed). This and other angular distributions to be discussed were obtained under conditions in which the projectile beam current measured on the target entrance grid was approximately neutralized by a low-energy electron beam current emitted by a nearby heated filament. Although not required, we find that the transmitted ion current is most stable when electrons are present.

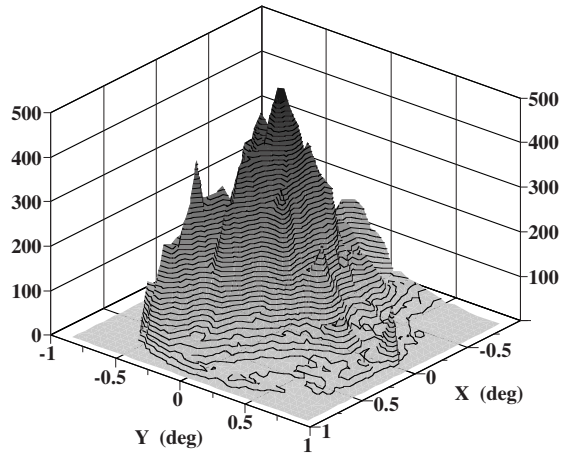

FIG. 2. Isometric view of the 2D angular distribution for 140 keV Ne^{7+} ions transmitted by the nanocapillary array ($2° \times 2°$) where the pores and beam direction are approximately aligned. A one-dimensional cut and projection is shown in Fig. 5(a).

The structure in the 2D angular distribution (Fig. 2) was further explored by rotating the target array with respect to the ion beam direction. Angular distributions obtained for the pores rotated beam-right by 0.10° and 0.20° in the $+X$ direction are shown in Figs. 3 and 4, respectively. Comparing Figs. 2–4 we see that these target movements appear to enhance some observed structure and steer the transmitted beam substantially toward the right. The transmitted yield decreased about 5% for each angular step. Target rotations in the opposite direction steer observed structure toward the left ($-X$ direction). The 0.1° target rotation angle is about equivalent to the nanopore aspect ratio ($D/L=1/600$). In most cases the 2D angular structure is repeatable on a given day (same incident beam tune and collimation slit settings) when the goniometer is returned to its initial location; differences are noted on different days following a 12 h period of no beam on target and a different beam tune. In general, the

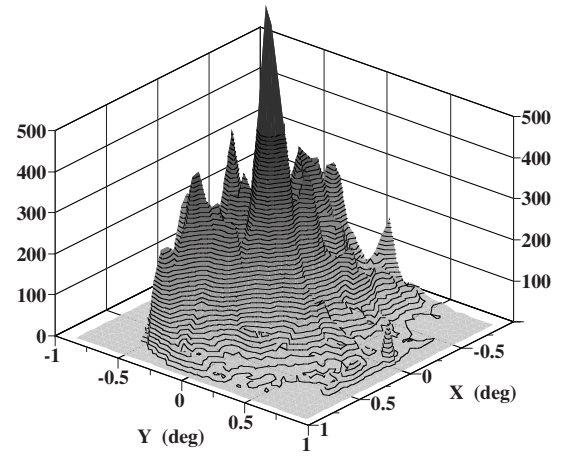

FIG. 3. Isometric view of the 2D angular distribution for 140 keV Ne^{7+} ions transmitted by the nanocapillary array ($2° \times 2°$) where the target is rotated 0.10° in the X direction from that used for Fig. 2. A one-dimensional cut and projection is shown in Fig. 5(b).

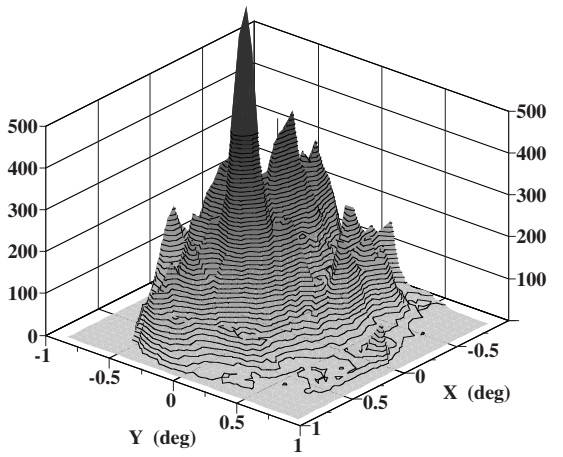

FIG. 4. Isometric view of the 2D angular distribution for 140 keV Ne^{7+} ions transmitted by the nanocapillary array ($2° \times 2°$) where the target is rotated 0.20° in the X direction from that used for Fig. 2. A one-dimensional cut and projection is shown in Fig. 5(c).

observed structure is found to be most distinct for ions at the highest projectile energies in the range 10–20 keV/q (i.e., for the highest projectile charge states at a fixed acceleration potential). Many target-beam alignment experiments suggested that it is not practical to achieve an alignment where the transmitted angular distribution contains no structure. But it is possible to obtain alignments where the angular structure is eliminated at least over a limited region of the full distribution, for example, in a narrow cut of fixed Y when the target is rotated in the X direction.

Comparison of the complicated 2D angular distributions obtained for 140 keV Ne^{7+} ions is simplified by examining slices of Figs. 2–4, projected along the horizontal direction (X axis); the projections are shown in Figs. 5(a)–5(c), respectively. The projection mask used, which encompasses the most intense part of each distribution, is shown in the insert of Fig. 5(a). The slice shown in Fig. 5(a) is a relatively smooth and broad angular distribution symmetric about the incident beam direction. The distribution width for transmitted ions is 50–100 times larger than the angular divergence of the incident beam (≈0.02° FWHM). The growth in beam width could be caused by multiple ultragrazing collisions with the charged nanopore walls (especially those that occur near the exit opening) as suggested schematically in Fig. 6(a). The increased divergence for transmitted ions may also be mirroring (in part) the effective small angular dispersion of nanopore directions within the limited region of the target being illuminated, as ions are reflected from the walls of pores. These wall collisions would have to occur at relatively large impact parameters, otherwise, the incident charge state fraction would have decreased as the ions traversed the nanopore channels. It is known that in grazing collision studies involving an insulator surface that HCIs capture electrons for impact parameters smaller than about 10 nm [23,24].

The bold structured distribution in Fig. 5(b) corresponds to the nanopores rotated by 0.1° toward the right along the X direction. This distribution is radically different and asymmetric compared to the Fig. 5(a) projection also superposed

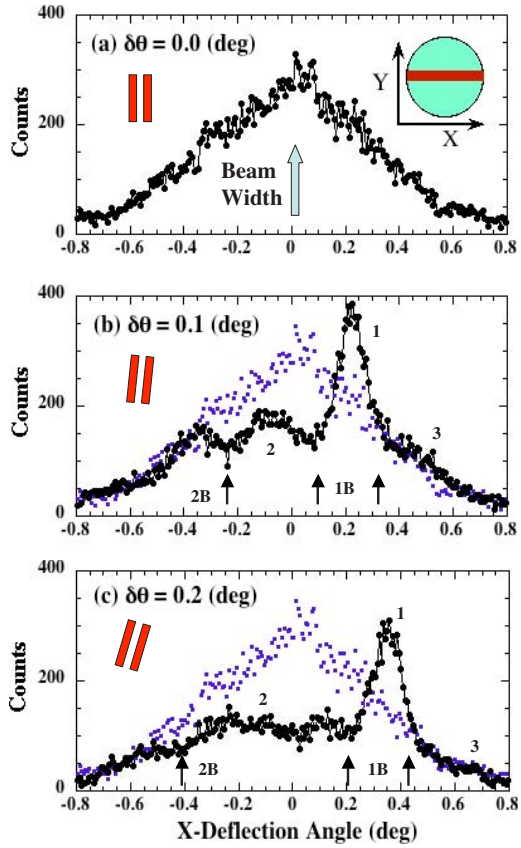

FIG. 5. (Color online) Narrow slices of three 2D angular distributions projected along the X direction (see inset) show the effects of 1D target rotations: (a) nanopores aligned to the beam direction; (b) nanopores rotated 0.1° toward the right, with projection (a) superposed in the background; (c) nanopores rotated 0.2° toward the right, with projection (a) superposed in the background. Peaks in (b) and (c) where single, double, and triple grazing collisions can contribute are labeled 1, 2, and 3, respectively. Arrows labeled 1B and 2B, where low yields occur, indicate the angles where single- and double-collision trajectories are blocked geometrically (see text and trajectories in Fig. 6).

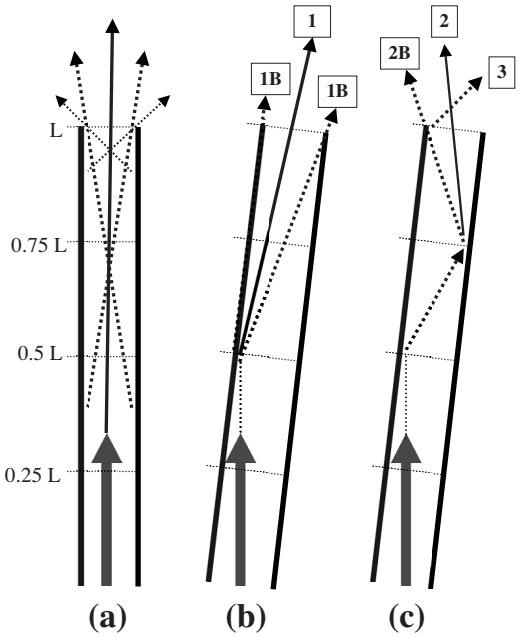

FIG. 6. Schematic view of ions bouncing inside nanopores when the pore direction is (a) aligned with the beam direction; (b) and (c) rotated clockwise by the capillary aspect ratio. Single collisions with the capillary wall are shown in (b); double collision events are shown in (c). Pore diameter D is greatly exaggerated relative to length L to illustrate trajectories that explain structure found in Fig. 5(b). Arrows labeled 1B and 2B, where low yields occur, indicate the angles where single- and double-collision trajectories are blocked geometrically.

in Fig. 5(b). It appears that the centroid of exiting ions in the broad peak of slice (a) moved about 0.2° along the X direction (i.e., by twice the target rotation angle toward the right) while the Y location of the intense 2D peaks in Fig. 3 remained fixed (Y projection not shown). An ion deflection angle that is twice the target rotation angle suggests that some projectile-wall collisions are specular. This strong peak at 0.2° labeled by "1" in slice (b), which corresponds to one ultragrazing bounce to the right from the left wall of nanopores as sketched in Fig. 6(b), has a width that approximately matches the angular width of the nanopore channels (≈0.1° FWHM). Peak "1" is also accompanied by the appearance of two broader low-intensity peaks. This structure will be explained later in terms of multiple grazing angle collisions (deflection right and then left) as ions traverse the long pores.

Similarly, a total target rotation angle displacement of 0.2° (from that shown in Fig. 2 corresponding to beam alignment) produces the angular distribution shown in Fig. 5(c). Here, the shifted and enhanced peak labeled "1" is displaced by almost 0.4° from the centroid of Fig. 5(a) and it is accompanied by an oscillating structure different from that shown in Fig. 5(b) left of peak "1." Again, peak "1" is associated with a grazing collision with the left nanopore wall. Because 2D angular distributions associated with orientations Figs. 2–4, were produced using the same total incident beam exposure of 140 keV Ne^{7+} ions, the projections in Fig. 5 are also normalized with respect to each other.

D. Transient effects

Transient effects in the ion transmission yield are always observed at the start of experiments or after reorienting the target with respect to the beam. When the incident beam is shut off for up to 3 h (the longest shutoff time investigated) after an angular distribution measurement and then restored, the fractional transmitted ion yield returns to its former value immediately. The complicated structure in angular distributions usually repeats when the ion beam is restored, suggesting that electrical charges embedded in or on capillary walls do not rearrange quickly. After the target orientation is changed, for example, in a 0.2° 1D goniometer rotation, the transmitted ion yield immediately drops by about a factor of two and then slowly recovers with a time constant of about τ=170 s for a 9.5 nA incident beam current according to the relationship $I(t)/I_0=[1-\exp(-t/\tau)]$, where I_0 is the incident beam current measured on the target (see Fig. 7). The recovery time constant τ is found to be inversely proportional to I_0 for beams in the 1–20 nA range. The time constant, which is

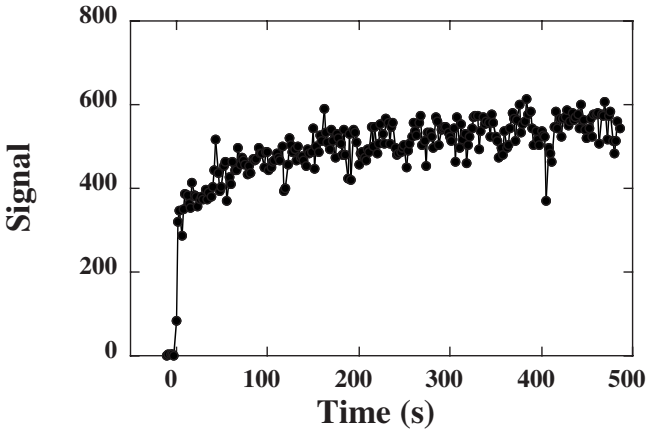

FIG. 7. Transient behavior of transmitted ions measured after a 0.2° angular displacement of the target. The transmitted signal immediately increases to about half of the equilibrium value when an incident beam current of 9.5 nA is introduced at $t=0$. The transient after $t=0^+$ fits the function $[1-\exp(-t/\tau)]$, where $\tau=170$ s (see the text).

independent of the presence or absence of electrons flooding the target, may be associated with charge rearrangement within the alumina pores after target reorientation, but we have no theory to explain the observed transient phenomena. Also, we find no evidence that the long-term transmitted ion fraction depends on the total ion dose deposited on the target array (i.e., no increased or decreased yield was apparent after about 60 h of 6–10 nA HCI beam exposure).

IV. ANALYSIS OF ANGULAR STRUCTURE

The rich angular structure observed in the 2D distributions (Figs. 2–4) and periodicity shown in Fig. 5 raised concern about the fine wire mesh mounted on the front of the alumina capillary target. The presence of the mesh might cause the alumina target to become electrically charged in a periodic 2D pattern between mesh wires and less charged beneath the wires. Ion scattering from such a macroscopic periodically charged array might yield 2D focusing effects analogous to those observed in axial channeling angular distributions, caused in channeling by the 2D periodic arrangement of atomic strings [14]. To evaluate whether the 2D mesh is the root cause of the corrugated structure observed in angular distributions, we tested arrays having uniform 7- and 14-nm-thick Au films deposited on the entrance surface and others with the films deposited on both sides. During Au deposition, the nanopore longitudinal direction was oriented at 45° with respect to the Au beam direction to limit Au deposition inside nanopores. Transmission experiments using these targets show that the total transmitted yield increases about a factor of 10–20 times compared to the wire mesh (for either single or double-sided coatings), which suggests that some target charging inhibits ion transmission only when the mesh is present. But these measurements, results of which will be published separately [22], also yield highly structured angular distributions and ion steering characteristics identical to those obtained for the capillary target with the mesh. We conclude that observed structure in transmitted ion angular distributions (Figs. 2–4) is primarily a characteristic of transmission through the (charged) porous alumina target and that the deposited metallic film is mainly a means of controlling the transmitted ion fraction.

The observation of structured angular distributions (Figs. 2–5) for low-energy ions scattered by a porous target of nanometer dimensions also raised the question about whether some structure could be the consequence of wave mechanical effects. For diffraction, the de Broglie wavelength $\lambda=h/p$ must be comparable to characteristic distances in the target, where h is Planck's constant and p is the projectile momentum. The longest wavelength associated with any of our measurements, corresponding to 10 keV Ne^+ ions ($v=\approx 3.1\times 10^5$ m/s), is of order 6×10^{-14} m. Because the smallest target dimension (of order 1 nm for the Al_2O_3 structure) is much larger than this wavelength, projectile deflection due to ion diffraction would not be resolved in our experiments ($\lambda/d\approx 6\times 10^{-5}$ radians or 3.5×10^{-3} degrees). (The equivalent deflection angle for 140 keV Ne^{7+} ions is about 3.7 times smaller.) Moreover, the observed spacing of the structures in our angular distributions is found to be independent of the projectile ion speed (i.e., momentum). Electrons from the projectile or the target also were not observed. Thus we can conclude that the presence of wave mechanical effects in any of our measured angular distributions is unlikely. Failures to explain the structured angular distributions by these considerations or from effects caused by the use of the wire mesh led us to focus on the effects of multiple grazing trajectories.

All of the interesting detail shown in Fig. 5(b) can be explained simply by single grazing reflections in ion wall collisions, multiple collisions, and trajectory blocking using geometrical analysis and numbered trajectories shown in Fig. 6. The angular width of the incident beam ($\approx 0.02°$) is small compared to the capillary aspect ratio ($D/L=1/600$, where the pore diameter and length are D and L, respectively). When the target is tilted by an angle ϑ to the right beyond the aspect ratio, $\vartheta=\tan^{-1}(D/L)\approx 0.10°$, the incident beam entering the pore is completely blocked in the 0° exit direction, and charge can deposit on the left wall of capillaries. Geometry suggests that the deposited charge centroid could be at $z=L/2$ as shown in Fig. 6(b), where z is the longitudinal coordinate measured from the upstream pore entrance and the measured blocking angles designated "1B" of 0.1° and 0.3° verifies the correctness of that assumption. This effective charge center also assumes that the incident beam was not deflected by preexisting charge patches located on capillary walls. Single bounce ions scattered near $z=L/2$ that can escape the tube (designated by "1" in Figs. 5 and 6), will show an average total deflection of $\vartheta+\tan^{-1}(D/L)=2\vartheta$. The single bounce ions deflected at angles larger than 2ϑ can undergo a second grazing collision from the right wall (opening a new scattering branch toward the left) as shown in Fig. 6(c). A fraction of those hitting the wall near $z=L$ can appear symmetrically in the vicinity of $\vartheta-\tan^{-1}(2D/L)=-0.10°$ and in general, be detected in region "2" (small peak) shown in Fig. 5(b). These transmitted double-collision grazing trajectories have second-collision impact points in the range 0.75

$<z<L$ on the right wall and are detected in region "2" (small peak centered about −0.10°). Those having a second impact point for $z<0.75L$, are blocked by the left capillary wall near the deflection angle, $\vartheta-\tan^{-1}(4D/L)=-0.28°$, about where a minimum labeled "2B" is shown in Fig. 5(b) and Fig. 6(c). Ions associated with this blocking dip will then give rise to a new low-intensity scattering branch (a fraction of the measured ions in the dip) toward the right, and these triple grazing collision ions begin appearing on the right wing of peak "1" at laboratory angles above 0.1 $+\tan^{-1}(4D/L)=0.48°$, labeled region "3" in Fig. 5(b). Examining the intensity here, we see in fact, a very small enhancement in the wing due to these triple collisions, in excess of the intensity found at the same angle in Fig. 5(a). Therefore, the observed dips at +0.1° and −0.25° in Fig. 5(b) adjacent to the region "2" can be explained geometrically by single and double bounce blocking, respectively. The fact that the dips are weak is probably evidence that many multiple collisions inside the pore do not have the specific impact points discussed above. While many ion-wall collisions probably occur near the nanopore entrance (i.e., before the "first collision" discussed above), these early collisions do not yield a clear intense transmitted signature in the angular distribution during the target tilting experiments (i.e., using 60-μm-thick Whatman target samples).

In the analysis, we should recognize that an even number of steered grazing collisions, each with an identical incident and reflection angle would actually result in scattered flux appearing at 0°, where single grazing collisions are blocked by pores rotated by >0.1°. Some transmitted double-collision flux at 0° is seen in Fig. 5(b). The double-collision flux appearing in region "2" is from ions not having identical reflectance angles in first and second wall collisions. The longitudinal distribution of first and second impact points also allows total ion deflection below 0°. Specifically, many first collisions do not impact at the $z=L/2$ centroid location and the actual deflection angles leaving any wall collision will most likely be distributed because of varying amounts of charge deposited on the capillary wall vs z. A distribution of ion-wall impact parameters will broaden structure in angular distributions, as well. We also note that the reflection and dip angles presented above are not complicated by the well-known self-image force induced when a grazing HCI is in the vicinity of a metal or insulator surface [23,24] because the q state of incident and reflected beams in each nanopore wall collision observed is identical (i.e., symmetric collisions). If we were considering a case where the projectile captures one or more electrons in the vicinity of the nanopore wall, then the change in rebound angle observed in HCI charge-changing grazing collisions due to that force (an asymmetric collision) would have to be included.

The same arguments can be made to explain the observed structure in Fig. 5(c) where the target tilt angle is 0.20° using slightly modified Figs. 6(b) and 6(c) drawings. Here, observed peak "1" is located at about 0.35° and the observed blocking angle minima (1B) are located at about 0.2° and 0.45°, respectively [see Fig. 5(c)]. Using these measured angles we calculate the effective centroid of the "first" wall interaction to be located at about $\langle z\rangle=2L/3$. For this location, second collisions hitting on the right wall at $z=L$ should rebound left and appear in the vicinity of +0.07° and extend toward negative laboratory angles. The two-collision blocking dip ("2B") should appear at about −0.37° as observed in Fig. 5(c) but the small three-collision peak ("3") expected at +0.77°, is less apparent in Fig. 5(c) compared to that seen in Fig. 5(b). Thus we see that the location of minima "1B," which located the effective charge center, self-calibrates the location of structure arising in higher-order collisions. The longitudinal location of the "first" wall interaction may move during small tilt experiments because of uncontrolled sample charging that deflects the incident beam. In all cases for our targets, the effective location for the first bounce observed was always relatively close to midway between the pore ends. Therefore, we always observe an approximate 2ϑ scaling for the main scattered peak observed ("1").

V. OTHER RESULTS

In general, 2D angular distributions similar to those shown in Figs. 2–4 (but usually not identical) are also observed in studies of Ar^{q+} ($q=1$, 3, and 7) and Ne^{q+} ($q=3$ and 7) at 10 keV/q. The total width of the "broad continuum" for each angular distribution approximately matches that of Ne^{7+} at 20 keV/q, as the projectile energy is decreased and for different projectile species and q state. However, the width of individual peaks within the 2D distribution measured for 30 keV Ne^{3+} and Ar^{3+} (approximately identical) are about 2 times broader than those for 140 keV Ne^{7+}, shown in Fig. 3 for the same incident beam collimation, so the structure becomes less pronounced at the lower energies. (A more poorly collimated incident beam at any energy also broadens the observed structure.) Structures in the 10 keV Ar^{+} angular distributions are about 50% broader still than those obtained at 30 keV. Therefore, the width of the most intense peaks in angular distributions is approximately inversely proportional to the projectile velocity. Surprisingly, 30 keV Ar^{3+} and 140 keV Ne^{7+} distributions measured on different days but with the incident beam constrained using the same collimation slit settings and goniometer orientation even displayed the same three intense 2D peak locations (within a few percent), after scaling the electrostatic deflection voltage (10 keV/q vs 20 keV/q).

One-dimensional steering of transmitted peaks by up to about ±2° with respect to the incident beam direction (shift of ±1° target rotation angle along the X-axis direction with respect to Fig. 2) was also studied for 140 keV Ne^{7+}, 60 keV Ne^{3+}, and 20 keV Ne^{+} ions. These larger 1D tilts in the X direction were accompanied by small shifts in the Y direction as well (few %). For peak shifts beyond ±2° from the starting alignment, large decreases in the transmitted yield per nA of incident ion beam occur (i.e., a factor of 2 or more decrease). This drop in yield with increasing pore misalignment may be caused by the increased number of grazing wall collisions that are required to steer ions to larger angular displacements. Studies performed at the larger tilt angles also required the rotation of the TDPSD in the X direction to track the steered peaks. No fundamental differences in the steering characteristics were observed for different charge-state species or projectile energy indicating, for example, that slower

ions do not exhibit an expanded steering range, at least in our 10–20 keV/q energy regime. These observations and other alignment experiments suggest that the angular distribution of nanopores inherent in the target may control the effective steering range.

The fractional population in each exit charge state for 30 keV Ar^{3+} was also studied vs alignment of the pore direction with the incident beam. The observed exit charge fractions for $q=3$, 2, and 1 states of 94.8%, 3.2%, and 2.0%, respectively, did not vary outside of statistical error for goniometer rotations studied of up to 1° (i.e., 2° total beam scattering) from the "best" nanopore orientation. As expected for our relatively low incident projectile speeds, we also detected no evidence of any transmitted charge state above the incident charge state for any projectile species, charge state, or incident energy.

VI. DISCUSSION AND CONCLUSIONS

In extensive investigations, the high-porosity ($f \approx 40\%$) 60-μm-thick × 100-nm-diam nanocapillary membrane made by Whatman, Inc. was shown to possess interesting ion transmission characteristics for a parallel incident beam of HCIs in the 10–20 keV/q energy range when studied using a detector with high angular resolution. The incident charge state is essentially the only transmitted ionic species (>20:1) and the width of the angular distribution envelope is typically <2 deg for any incident charge state, projectile, and energy studied. The angular distribution width of about 0.8° FWHM measured for 140 keV Ne^{7+} ions [(Fig. 5(a)] suggests that the angular spread in the longitudinal direction of nanopores for the Whatman samples is relatively narrow; the results of other tilting experiments performed using a 200 MeV Ti^{12+} ion beam [21] are consistent with this interpretation. As demonstrated in low-energy target tilting experiments (Figs. 2–5), the surprising narrow peaks in the angular distributions appear to be caused by the 2D dispersion of nanopore orientations in the sample and elastic multiple collisions with the charged nanopore walls. The narrow peaks observed do not appear to be dependent on the incident q state or ion beam dose once the transmitted current reaches a steady-state maximum value (i.e., following transient buildup). The angular width of the sharp peaks in angular distributions is equivalent to the nanopore aspect ratio (1/600) for a parallel beam of 140 keV Ne^{7+} ions, but we find that their width increases slowly for slower projectile ions (approximately as v^{-1}) or when more divergent incident beams are used. The most prominent structure observed in the angular distribution (Fig. 5), associated with single specular collisions with a nanopore wall, always shifts approximately by 2× the sample tilt angle over a range studied of about ±1°. Smaller peaks identified in tilting experiments were shown to be the consequence of double or triple collisions with the wall.

The surprisingly low transmitted ion fraction observed in our 10- to 20-keV/q energy regime is found to be in the range 3×10^{-7} or 3×10^{-8} depending on whether target surfaces are coated with thin Au films or a high-transmission grid on the beam incident surface, respectively. Optimization of this transmitted fraction (particle nA) in the incident charge state is found to be a reliable method for orienting the longitudinal direction of nanopores to the beam direction. The very low fraction of transmitted current and other characteristics observed using these thick Whatman alumina arrays indicates that they can be used as a beam attenuator for incident HCI ion beam currents up to 20 nA in the intermediate energy regime; the transmission characteristics have not been studied at significantly larger incident beam current, but some interesting preliminary results obtained for Au-clad Whatman arrays using low-intensity HCI beams in our laboratory have been reported [22].

Our results contrast sharply with the experimental results obtained in short (10 μm) PET film target studies using much slower incident 3 keV Ne^{7+} ions (0.35 keV/u), where the high-transmission "ion guidance" mechanism was identified and studied [7–11]. For example, the PET film studies found a large transmitted fraction (0.5 vs $<2\times10^{-7}$ here), broad unstructured angular distributions (vs highly structured distributions here), and a strong observed transient effect (vs a weak effect here). In addition, the PET angular distribution centroid moved differently than present experiments when the target is tilted (ϑ vs 2ϑ here, where ϑ is the tilt angle). Further explanation of the present results will have to await new theoretical calculations applied to ion transmission in long Al_2O_3 pores. Thus far, contrasting theoretical approaches have been applied only in the study of the 10-μm-thick PET (insulator) films by Stolterfoht *et al.* [7–9] and by Burgdörfer and co-workers using a general method [12].

ACKNOWLEDGMENTS

We are indebted to Hans M. Christen of the ORNL Materials Science and Technology Division for applying gold films on some nanocapillary targets mentioned in these studies. This research was sponsored by the Office of Basic Energy Sciences of the U.S. Department of Energy under Contract No. DE-AC05-00OR22725 with UT-Battelle, LLC.

[1] G. P. Crawford, L. M. Steele, R. Ondis-Crawford, G. S. Iannacchione, C. J. Yeager, J. W. Doane, and D. Finotello, J. Chem. Phys. **96**, 7788 (1992).
[2] D. Marchal and B. Demé, J. Appl. Crystallogr. **36**, 713 (2003).
[3] Y. Yamazaki *et al.*, J. Phys. Soc. Jpn. **65**, 1199 (1996).
[4] S. Ninomiya, Y. Yamazaki, F. Koike, H. Masuda, T. Azuma, K. Komaki, K. Kuroki, and M. Sekiguchi, Phys. Rev. Lett. **78**, 4557 (1997).
[5] Y. Yamazaki, Phys. Scr., T **T73**, 293 (1997).
[6] K. Tökési, L. Wirtz, C. Lemell, and J. Burgdörfer, Phys. Rev.

A **61**, 020901 (2000).
[7] N. Stolterfoht, J. H. Bremer, V. Hoffmann, R. Hellhammer, D. Fink, A. Petrov, and B. Sulik, Phys. Rev. Lett. **88**, 133201 (2002).
[8] N. Stolterfoht, V. Hoffmann, R. Hellhammer, D. Fink, A. Petrov, Z. D. Pêsic, and B. Sulik, Nucl. Instrum. Methods Phys. Res. B **203**, 246 (2003).
[9] N. Stolterfoht, R. Hellhammer, P. Sobocinski, Z. D. Pêsic, J. Bundesmann, A. Petrov, B. Sulik, M. B. Shah, K. Dunn, J. Pedregosa, and R. W. McCullough, Nucl. Instrum. Methods Phys. Res. B **235**, 460 (2005), and other recent references contained therein.
[10] Y. Kanai (private communication).
[11] F. Aumayr (private communication).
[12] J. Burgdörfer, C. Lemell, K. Schiessl, B. Solleder, C. Reinhold, K. Tökési, and L. Wirtz, in *Photonic, Electronic, and Atomic Collisions*, Proceedings of the XXIV International Conference, Rosario, Argentina, edited by Pablo D. Fainstein, Marco Aurelio P. Lima, Jorge E. Miraglia, Eduardo C. Montenegro, and Roberto D. Rivarola (World Scientific, Singapore, 2006), pp. 16–45.
[13] Gy. Vikor, R. T. Rajendra Kumar, Z. D. Pêsic, N. Stolterfoht, and R. Schuch, Nucl. Instrum. Methods Phys. Res. B **233**, 218 (2005).
[14] Herbert F. Krause and Sheldon Datz, "Channeling Heavy Ions through Crystalline Lattices," *Advances in Atomic, Molecular, and Optical Physics*, edited by B. Bederson (Academic Press, New York, 1996), pp. 139–180.
[15] A. A. Greenenko and N. F. Shul'ga, Nucl. Instrum. Methods Phys. Res. B **205**, 767 (2003).
[16] H. Masuda, H. Yamada, M. Satoh, Hidetaka Asoh, M. Nakao, and T. Tamamura, Appl. Phys. Lett. **71**, 2770 (1997).
[17] O. Painter and K. Srinivasan, Phys. Rev. B **68**, 035110 9 (2003).
[18] S. M. Cooper, B. A. Cruden, M. Meyyappan, Reni Raju, and S. Roy, Nano Lett. **3**, 1701 (2003).
[19] Z. L. Xiao, C. Y. Han, U. Welp, H. H. Wang, W. K. Kwok, G. A. Willing, J. M. Hiller, R. E. Cook, D. J. Miller, and G. W. Crabtree, Nano Lett. **2**, 1293 (2002).
[20] Nanopore membranes are available from Whatman Inc., 200 Park Avenue, Ste. 210, Florham Park, NJ 07932 USA.
[21] H. F. Krause, C. R. Vane, F. W. Meyer (unpublished).
[22] H. F. Krause, C. R. Vane, F. W. Meyer, and H. M. Christen, in Journal of Physics: Conference Series 58, Proceedings of the 13th International Conference on the Physics of Highly Charged Ions, Queens University, Belfast, Northern Ireland, UK, edited by R. W. McCullough, F. J. Currell, G. Gribakin, and M. P. Scott (IOP Publishing, Belfast, 2007), pp. 323–326.
[23] F. W. Meyer, L. Folkerts, H. O. Folkerts, and S. Schippers, Nucl. Instrum. Methods Phys. Res. B **98**, 441 (1995).
[24] J. J. Ducrée, F. Casali, and U. Thumm, Phys. Rev. A **57**, 338 (1998).